

Global axisymmetric simulations of two-fluid reconnection in an experimentally relevant geometry

Nicholas A. Murphy*

*Department of Astronomy and the Center for Magnetic Self-Organization in Laboratory and Astrophysical Plasmas,
University of Wisconsin, Madison, Wisconsin, 53706*

Carl R. Sovinec

*Department of Engineering Physics and the Center for Magnetic Self-Organization in Laboratory and Astrophysical Plasmas,
University of Wisconsin, Madison, Wisconsin, 53706*

(Dated: January 22, 2008)

To address the interplay between local and global effects in magnetic reconnection, axisymmetric numerical simulations for the Magnetic Reconnection Experiment [M. Yamada *et al.*, Phys. Plasmas **4**, 1936 (1997)] are performed using the NIMROD code [C.R. Sovinec *et al.*, J. Comp. Phys. **195**, 355 (2004)]. The ‘pull’ and ‘push’ modes of the device are simulated both with and without two-fluid effects in the generalized Ohm’s law. As in experiment, the pull reconnection rate is slowed due to the presence of downstream pressure associated with the outflow. Effects induced by toroidicity include a radially inward drift of the current sheet during pull reconnection and a radially outward displacement of the X-point during push reconnection. These effects result from the inboard side of the current sheet having less volume than the outboard side, facilitating the formation of large scale pressure gradients since the inboard side is more susceptible to a buildup or depletion of density. Toroidicity also leads to asymmetry of the quadrupole field during two-fluid simulations. During pull reconnection, the outboard lobes of the quadrupole typically peak close to the X-point, whereas the inboard quadrupole lobes peak near the flux core surfaces. At experimentally relevant parameters, the reconnection rate is found to depend more on the mode of operation than on the inclusion of two-fluid effects. The current sheet in two-fluid co-helicity simulations tilts due to a Lorentz force associated with the guide field and the outflowing electrons, resulting in asymmetric flow patterns for both ions and electrons. In two-fluid counter-helicity simulations, the Hall effect leads to a radial shift in position of the X-point and an asymmetric outflow pattern, which is examined in terms of separate force-density contributions. In general, asymmetry due to toroidicity or the Hall effect often leads to uneven outflow, which then feeds back on the reconnection process through large scale pressure gradients.

PACS numbers: 52.35.Vd, 52.65.-y

Keywords: Magnetic reconnection, plasma simulation, Hall effect, plasma magnetohydrodynamics

I. INTRODUCTION

Magnetic reconnection is the process through which the topology of magnetic field lines in a highly conducting plasma is changed. In recent years, it has been realized that two-fluid effects, in particular the Hall term in the generalized Ohm’s law, often play a key role in facilitating the reconnection process [1]. The properties of the electron outflow have been linked with the dispersive properties of the whistler and kinetic Alfvén waves, in particular that $\omega \sim k^2$. The phase velocity of the wave increases for shorter length scales, allowing a constant outflow of electrons almost independent of the width of the outflow region [2]. This also makes the reconnection rate almost independent of the mechanism that breaks the frozen-in condition (e.g. Ref. 3).

A readily apparent feature of two-fluid antiparallel magnetic reconnection is the out-of-plane quadrupole magnetic field. On length scales shorter than the ion in-

ertial length c/ω_{pi} , electrons and ions become decoupled. On these scales, the ions respond sluggishly while the electrons are able to respond quickly. The result is that the magnetic field becomes tied to the electrons rather than the bulk plasma. This allows the out-of-plane electron flow associated with the reconnecting current to pull in-plane magnetic field lines in the out-of-plane direction, resulting in the familiar quadrupole pattern [3, 4]. The shape of the quadrupole in simulations depends on the plasma parameters, the problem setup, and the choice of physical model. In hybrid simulations with kinetic ions and fluid electrons, for example, the quadrupole field tends to be much broader and less strongly peaked than in Hall MHD simulations [5].

The Magnetic Reconnection Experiment (MRX) [6] is located at the Princeton Plasma Physics Laboratory and is designed to study controlled nearly axisymmetric reconnection. The extensive list of results from this device include work on the shape of the current sheet [7], verification of a generalized Sweet-Parker model [8], studies of ion heating [9, 10] and lower-hybrid drift turbulence [11, 12], the measurement of the transverse and parallel Spitzer resistivities [13, 14], an investigation of electro-

*Electronic address: murphy@astro.wisc.edu

magnetic fluctuations in the current sheet [15–17], active perturbation of the current sheet [17], and a study of the formation, stability, and sustainment of field-reversed configurations [18, 19]. A 2004 upgrade to the device gave MRX the capability to investigate lower collisionality plasmas [20, 21] and to change the flux core separation [22, 23]. Recent work has focused on two-fluid effects in reconnection, including observations of the quadrupole field [20, 21, 24] as well as symmetry breaking due to the Hall effect during counter-helicity push reconnection [25]. We note that the out-of-plane quadrupole magnetic field has also been observed during counter-helicity spheromak merging in the Swarthmore Spheromak Experiment (SSX) [26] and in spacecraft observations of the Earth’s magnetosphere (e.g. Ref. 27).

Most two-fluid and particle-in-cell (PIC) simulations of reconnection are restricted to a simplified geometry (e.g. Ref. 1), and most global simulations in a realistic geometry focus primarily on resistive MHD (e.g. Refs. 28–30). In the present work, we extend previous efforts by including two-fluid effects in global simulations of reconnection in an experimentally relevant geometry. This allows a detailed investigation of the coupling between the small scale physics of the diffusion region and the large scale magnetic field geometry.

The MRX experiment has been simulated previously by two groups. Reference 28 reports island formation during co-helicity merging with a spatially nonuniform resistivity. Reference 30 uses the TRIM code (TRIangular Magnetohydrodynamics) [31] to simulate co- and counter-helicity pull reconnection in MRX. This group adds a ‘model Hall’ term which, due to stringent time-step limitations, is limited to one-sixth of the true strength of the Hall term. Our simulations extend previous work to fully include the Hall effect with a focus on the role of global effects during the reconnection process.

MRX, unlike the earlier reconnection experiments of Stenzel and Gekelman [32], drives reconnection through toroidal flux cores. We would normally expect toroidicity to be unimportant because the width δ of the reconnection layer is much less than the major radius R , especially during pull reconnection. However, our simulations show that toroidicity has noticeable effects on the reconnection process. In pull reconnection, for example, the inboard side of the current sheet becomes depleted of density more quickly than the outboard side due to the smaller available volume, resulting in asymmetric inflow. While most studies of reconnection either assume or find the process to be symmetric to a 180° rotation about the center of reconnection, some recent work has explicitly studied reconnection with asymmetric inflow [33–38].

The choice of MRX as the basis for an investigation of the interplay between local and global effects in reconnection is advantageous due to the well-understood experimental setup and the availability of laboratory data. In addition, the plasma parameters are not too extreme for direct simulation. Our goal is not to simulate MRX in detail, but rather to use the geometry and setup of the

device to investigate the role of global effects during the reconnection process.

In Sec. II we describe the two-fluid and resistive MHD models used in our simulations of MRX. In Sec. III we provide an overview of the simulation setup as well as initial and boundary conditions for our model of MRX. Sections IV and V present simulation results for antiparallel resistive MHD and two-fluid reconnection, respectively, and provide a discussion of the relevant physics. Section VI contains details of two-fluid co- and counter-helicity simulations of reconnection in MRX. Section VII contains a summary and concluding remarks.

II. TWO-FLUID MODEL

The NIMROD (Non-Ideal Magnetohydrodynamics with Rotation, Open Discussion) code [39] solves the equations of two-fluid MHD cast in a single-fluid form. The solution is represented by a quadrilateral finite element mesh in the poloidal plane and a finite Fourier series in the toroidal direction. However, all simulations performed specifically for this paper are axisymmetric. The semi-implicit leapfrog time advance allows the full inclusion of the Hall term without a severe time step limitation [40, 41].

The combined Faraday/Ohm’s Law in our model is given by

$$\frac{\partial \mathbf{B}}{\partial t} = -\nabla \times \left(\eta \mathbf{J} - \mathbf{V} \times \mathbf{B} + \frac{\mathbf{J} \times \mathbf{B}}{ne} - \frac{\nabla p_e}{ne} \right). \quad (1)$$

The choice for resistivity of $\eta = 10^{-4} \Omega \cdot \text{m}$ ($\eta/\mu_0 = 80 \text{ m}^2 \text{ s}^{-1}$) corresponds to the parallel Spitzer resistivity for a plasma with an electron temperature of $T_e = 15 \text{ eV}$. A scalar electron pressure is assumed, so potentially important effects associated with the off-diagonal terms in the electron pressure tensor are absent. These missing effects may alter the structure of the electron diffusion region, although the reconnection rate is expected to remain unaffected [1]. Because the electron inertial length $c/\omega_{pe} \sim 1 \text{ mm}$ is small compared to a resistive skin depth of a few centimeters, we neglect electron inertia in these simulations. Investigations in the SSX device have also noted that in the reconnection region, the electron inertia term will be orders of magnitude smaller than the resistive term [42]. No hyperresistivity is used, leaving resistivity as the sole mechanism that breaks magnetic field lines.

For the resistive MHD simulations reported in Section IV of this paper, Eq. (1) reduces to

$$\frac{\partial \mathbf{B}}{\partial t} = -\nabla \times (\eta \mathbf{J} - \mathbf{V} \times \mathbf{B}). \quad (2)$$

Ampere’s Law without displacement current is

$$\mu_0 \mathbf{J} = \nabla \times \mathbf{B}. \quad (3)$$

The divergence constraint is

$$\nabla \cdot \mathbf{B} = 0. \quad (4)$$

Because this condition is not met exactly by the numerical representation, a divergence cleaning technique is used [39]. The momentum equation with viscosity is given by

$$\rho \left(\frac{\partial \mathbf{V}}{\partial t} + \mathbf{V} \cdot \nabla \mathbf{V} \right) = \mathbf{J} \times \mathbf{B} - \nabla p + \nabla \cdot \rho \nu \nabla \mathbf{V}. \quad (5)$$

The coefficient for viscosity is given by $\nu = 80 \text{ m}^2 \text{ s}^{-1}$. Continuity is given by

$$\frac{\partial n}{\partial t} + \nabla \cdot (n \mathbf{V}) = \nabla \cdot D \nabla n. \quad (6)$$

The number density diffusivity D (chosen to be $80 \text{ m}^2 \text{ s}^{-1}$) is used primarily as a numerical smoothing parameter to ensure a well-behaved solution. For simplicity, the ion and electron temperatures are assumed to be equal. Temperature evolution is given by

$$\frac{n}{\gamma - 1} \left(\frac{\partial T}{\partial t} + \mathbf{V} \cdot \nabla T \right) = -\frac{p}{2} \nabla \cdot \mathbf{V} - \nabla \cdot \mathbf{q} + Q, \quad (7)$$

where $Q = \eta J^2 + \nu \rho \nabla \mathbf{V}^T : \nabla \mathbf{V}$ and $\mathbf{q} = n \chi \nabla T$ with a thermal diffusivity of $\chi = 400 \text{ m}^2 \text{ s}^{-1}$ in most computations. A comparison of results with anisotropic heat conduction ($\mathbf{q} = -n [\chi_{\parallel} \mathbf{b} \mathbf{b} + \chi_{\perp} (\mathbf{I} - \mathbf{b} \mathbf{b})]$ with $\chi_{\parallel} = 3 \times 10^5 \text{ m}^2 \text{ s}^{-1}$ and $\chi_{\perp} = 3 \times 10^2 \text{ m}^2 \text{ s}^{-1}$, where \mathbf{b} is a unit vector in the direction of the magnetic field) is discussed in Sec. V A.

NIMROD solves the equations of extended MHD, but does not contain all of the kinetic effects that are simulated in particle-in-cell codes. Notably absent are electron turbulence, particle demagnetization near field nulls, and acceleration of energetic particles. Nevertheless, other studies (e.g. Ref. 3) have shown that the reconnection rate is largely independent of the mechanism that breaks the frozen-in condition, so NIMROD is well-suited to investigate the interplay between local and global effects on the reconnection process. The two-fluid model used here has been successfully tested on a variety of benchmark problems, including the g-mode [41] and the two-fluid tearing mode [43].

III. MRX SIMULATION SETUP

The presence of dual flux cores requires that the computational domain be multiply connected. Hence it is untenable to use a logically rectangular mesh of quadrilateral finite elements to represent the poloidal plane. To generate the grid for MRX, the positions of the vertices of each element along the outer boundary are specified. The remaining interior element vertex positions are found through an iterative process where the new position of a vertex is found through a weighted average of

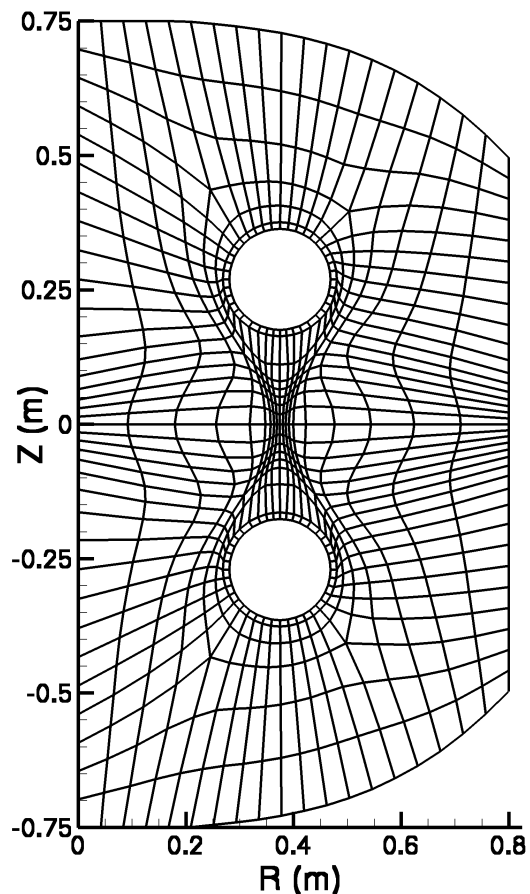


FIG. 1: A low resolution version of the finite element grid used for toroidal simulations of two-fluid pull reconnection in MRX. Note that high resolution is present both in the reconnection region and along the expected position of the quadrupole field.

the surrounding vertices. The weight function depends on position and is chosen to provide high resolution in regions of strong gradients (e.g. the current sheet and the quadrupole field regions). Different weight functions are chosen for different modes of operation and for different physical models. A low resolution version of the finite element grid used for two-fluid pull reconnection is shown in Fig. 1. For simulations with toroidicity, an approximation to the actual flux conserver shape is used as the outer boundary. Some simulations use linear geometry in order to isolate the effects of toroidicity and to simplify the analysis. In particular, Figs. 5, 6, 11, 12, 13, 14, and 15 all show results from linear geometry computations. For these simulations, a rectangular outer boundary is used. The flux cores are included in each of these geometries. All simulations presented here are axisymmetric and use bicubic finite element basis functions which are fourth order accurate when solutions are sufficiently smooth.

In ‘pull’ reconnection, magnetic flux surfaces are pulled into the flux cores. This setup is reminiscent of reconnection in the Earth’s magnetotail and in coronal mass

ejections. In the experiment, this results in a reconnection sheet with radial inflow and axial outflow. In ‘push’ reconnection, magnetic flux surfaces are pushed out of the flux cores. This results in axial inflow and radial outflow. A third mode of operation involving spheromak merging is not simulated in this paper. The majority of published results from the MRX device is from the pull mode of operation.

The initial magnetic field is set up through coils at the center of each flux core with positions and current $(R, Z, I) = (37.5 \text{ cm}, \pm 27 \text{ cm}, -50 \text{ kA})$, with vertical field coils at $(R, Z, I) = (89 \text{ cm}, \pm 121 \text{ cm}, 134 \text{ kA})$ for simulations with toroidal geometry. This sets a vacuum X-point at the midpoint between the two flux core positions. The initial field is purely poloidal. A toroidal electric field is applied on the flux core surfaces to induce poloidal magnetic field. Depending on the direction, this electric field drives either push or pull reconnection. In the experiment, some toroidal field is always generated during the plasma formation process; however, no toroidal field is induced directly by the flux cores in our null-helicity simulations. For the co- and counter-helicity simulations of push reconnection reported in Sec. VI, a poloidal electric field is applied to the flux core surfaces to induce a toroidal magnetic field in addition to the toroidal electric field. The duration of reconnection in experiment is $\sim 50 \mu\text{s}$, and the simulations represent $15 - 20 \mu\text{s}$ of this period. The magnitude of the applied voltage is chosen to give a reconnecting electric field comparable to that observed in experiment. Typical simulation parameters are shown in Table I.

Like previous simulations of MRX [28, 30], resistivity is enhanced around the flux core surfaces. The diffusivity profile used in this work is of the form

$$\frac{\eta}{\eta_0} = 1 + C_\eta \left[\exp\left(-\frac{(r_1 - r_c)^2}{(Ar_c)^2}\right) + \exp\left(-\frac{(r_2 - r_c)^2}{(Ar_c)^2}\right) \right], \quad (8)$$

where r_1 and r_2 are the distances from a point in the domain to the centers of the two flux cores and $r_c = 9.4 \text{ cm}$ is the flux core minor radius. The choices of the coefficients A and C_η are $A = 0.3$ and $C_\eta = 3$. Additional diffusivity shaping is used along the exterior of the domain to prevent the development of unresolved boundary layers. No diffusivity enhancement is used in the reconnection region in any of the simulations reported in this paper. Apart from the position dependence described above, the resistivity η is held constant and is not a function of temperature or current density.

The simulations assume perfectly conducting no-slip boundary conditions along the exterior wall. The normal component of velocity on the flux core surfaces is given by the $\mathbf{E} \times \mathbf{B}$ drift. The number density on the flux core surfaces is kept at the initial value of number density in the simulation. This is a reasonable approximation because the flux core surface can act both as a sink and source of material in the experiment. For consistency with much of the work reported by the experiment [20, 21], the ion species is assumed to be deuterium. With

TABLE I: Simulation Parameters

Initial Number Density	$5 \times 10^{19} \text{ m}^{-3}$
Initial Temperature	15 eV
Ion Species	D^+
Flux Core Loop Voltage (V_{loop})	1000 V
Characteristic Magnetic Field	350 G
Characteristic Length Scale ^a	25 cm
Characteristic Alfvén Speed (V_A)	75 km s^{-1}
Characteristic Sound Speed (V_S)	35 km s^{-1}
Thermal Diffusivity (χ)	400 $\text{m}^2 \text{ s}^{-1}$
Resistivity (η)	$10^{-4} \Omega \cdot \text{m}$
Viscosity (ν)	80 $\text{m}^2 \text{ s}^{-1}$
Lundquist Number (S)	240
Ion Inertial Length (c/ω_{pi})	4.5 cm

^aAn intermediate value between the current sheet length and the system size.

this choice of species, the ion inertial length is given by $c/\omega_{pi} = 4.5 \text{ cm}$.

IV. RESISTIVE MHD NULL-HELICITY SIMULATIONS

In this section we provide an overview and discussion of simulations of resistive MHD reconnection for both the push and pull modes of operation. Resistive MHD cases reproduce many global effects observed in the experiment and also provide instructive comparisons with the two-fluid simulations discussed in Sec. V. Because the initial magnetic field is purely poloidal and the applied electric field is purely toroidal, no mechanism in the resistive MHD framework exists to generate in-plane currents or out-of-plane magnetic field. Unless otherwise noted, all figures in this section are from $t = 11.2 \mu\text{s}$ after the start of each simulation, when the current sheet is well developed.

A. Resistive MHD pull reconnection

Simulations of resistive MHD pull reconnection with the plasma parameters listed in Table I result in a Sweet-Parker-like current sheet. The toroidal current density and plasma pressure are shown in Fig. 2. The width δ of the current sheet is found through a fit to the function

$$B_Z(R) = B_0 \tanh\left(\frac{R - R_0}{\delta}\right) + b_1(R - R_0). \quad (9)$$

The last term takes into account that B_Z does not approach a constant far from the current sheet. This is similar to the equation used in Ref. 44 to describe the neutral sheet profile. We define the length of the current sheet $L_{0.5}$ as the distance in the outflow direction between the peak of the reconnecting current and where the reconnecting current density reaches half of the peak value.

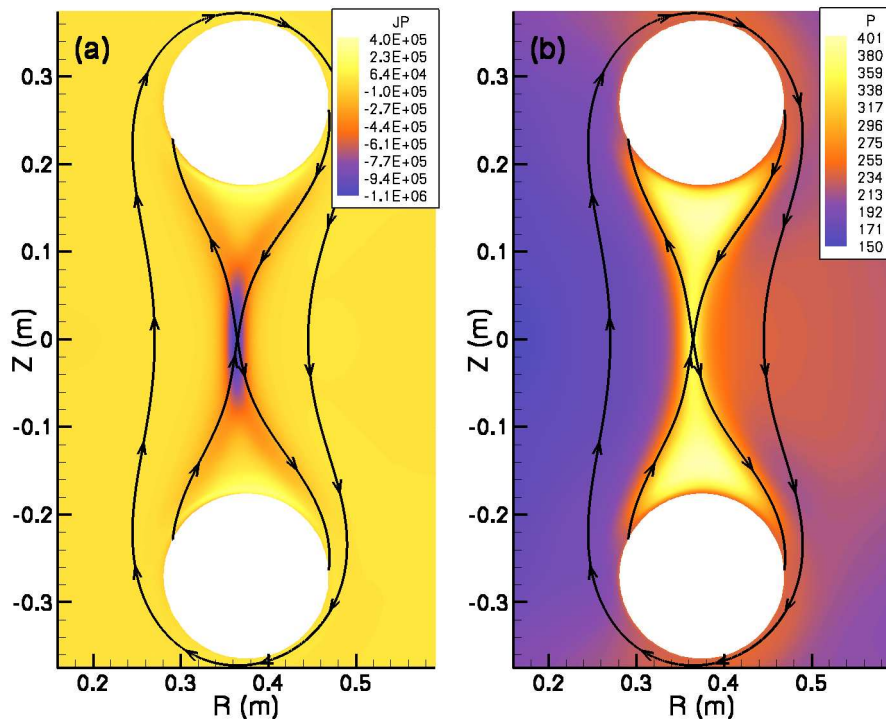


FIG. 2: Simulations of pull reconnection using a resistive MHD model show the development of Sweet-Parker-like current sheets. Shown are (a) the toroidal current density and (b) the plasma pressure (in SI units) along with streamtraces of the magnetic field.

For Fig. 2, we find that $\delta \approx 1.2$ cm and $L_{0.5} \approx 8$ cm. The outflow velocity is ~ 20 km s $^{-1}$. This is noticeably slower than $V_A \sim 75$ km s $^{-1}$ expected from Sweet-Parker theory due to the high downstream pressure [seen in Fig. 2(b)] that results from outflow being confined between the separatrixes and the flux cores. The ratio of downstream and central pressure to the inflow pressure produced in the simulation (roughly a factor of 2) is comparable to the ratio of densities shown in Fig. 8 of Ref. 45.

The inboard side of the current sheet has noticeably lower plasma pressure than the outboard side during pull reconnection in toroidal geometry, as evident in Fig. 2(b). This is a consequence of the lower volume on the inboard side than on the outboard side and leads to asymmetric inflow with a radially inward drift of the current sheet, which is discussed in more detail later in the section. The relatively low inboard pressure has also been observed in experiment [22]. With a sound speed of approximately 35 km s $^{-1}$, pressure does not equilibrate along magnetic field lines that encircle the flux cores from one inflow region to the other on the time scale of the driven transient. Thus, the flow stagnation point and the field null are not collocated during reconnection, as shown in Fig. 3.

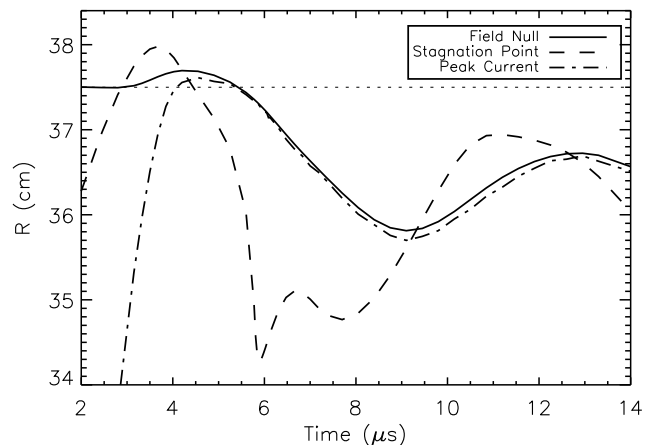


FIG. 3: The position of the field null, the flow stagnation point, and the maximum current density as a function of time during a null-helicity resistive MHD simulation of pull reconnection. Similar behavior is observed when the Hall term is included.

B. Resistive MHD push reconnection

Simulations of resistive MHD push reconnection in MRX's geometry (see Fig. 4) show a Sweet-Parker-like current sheet similar to those seen in pull reconnection. For most of the physical parameters tested, both the

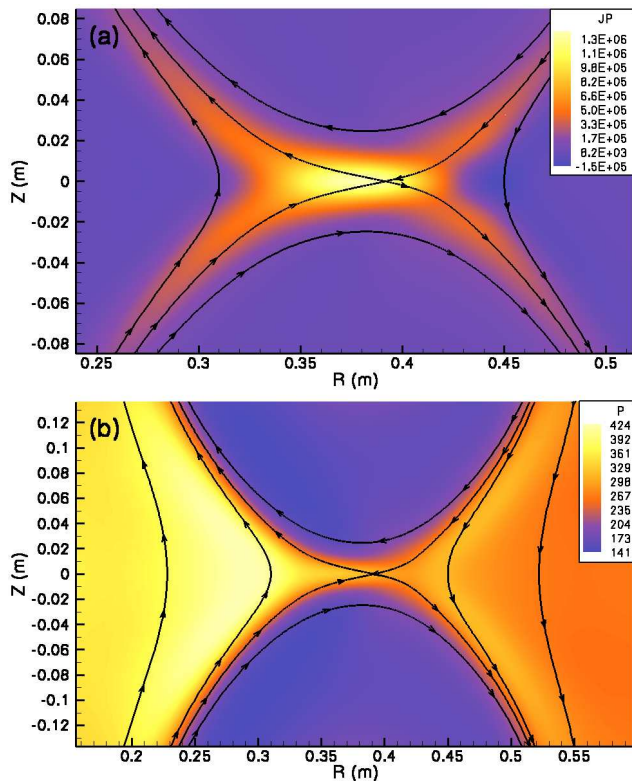


FIG. 4: Simulations of resistive MHD push reconnection in a toroidal geometry, showing (a) toroidal current density and (b) plasma pressure, along with streamtraces of the poloidal magnetic field.

length and width of the current sheet are shorter during push reconnection than during pull reconnection with the same magnitude of applied voltage. In Fig. 4, $\delta \approx 0.7$ cm and $L_{0.5} \approx 4.3$ cm, as found through the push reconnection analogue to Eq. (9). The inflow is symmetric about $Z = 0$, whereas the outflow is asymmetric in the radial direction due to toroidal effects. The position of the field null in Fig. 4 is near the outboard side of the current sheet. The inboard downstream region has significantly higher plasma pressure than the outboard downstream region. As in the case of pull reconnection, the radial position of the field null does not remain static and can be a short distance from the stagnation point. The outflow velocity patterns on the two sides of the X-point is not symmetric due both to toroidicity and the significant buildup of plasma pressure in the inboard downstream region.

C. Discussion of resistive MHD results

1. Asymmetric effects associated with toroidicity

In experiment and in previous simulations [30], it has been noted that the current sheet moves radially inward at a rate of a few kilometers per second during pull re-

connection. Quantitatively consistent radial motion is present in the null-helicity simulations reported in this paper. The radial position of the magnetic field null, the flow stagnation point, and the peak toroidal current density are all shown in Fig. 3. It is apparent that reconnection in these simulations occurs in a moving reference frame. Starting around $5 \mu\text{s}$, the field null moves inward at a maximum rate of 6 km s^{-1} before commencing radially outward motion at around $9 \mu\text{s}$. The flow stagnation point and the magnetic field null are not at the same position, except around times when the instantaneous velocity of the field null is zero. When the field null has an inward (outward) motion, the stagnation point is at a lower (higher) radius. The peak current density tends to be at a slightly lower radius than the field null.

To understand the cause of the radial drift, we note simulation conditions where it does not occur. First, this radial drift in position does not occur in $\beta = 0$ simulations, indicating that pressure effects are necessary. Second, this drift does not occur in MRX-like simulations in linear geometry with symmetric boundaries and finite β . In this case, the field null, the flow stagnation point, and the peak current density are collocated at the midpoint between the two flux cores. Comparing the simulation results, a large scale pressure gradient between the inboard and outboard sides of the reconnection region only develops in the finite β toroidal case where approximately even inflow from both sides of the current sheet depletes density from the inboard side more quickly than from the outboard side. This leads to the outboard side of the current sheet having a peak pressure which is 25-50% higher than on the inboard side, as can be seen in Fig. 2(b). This leads to a net inward radial force that pushes the current sheet to lower radii. An additional consequence is that the flow stagnation point is on the inboard side of the field null during inward motion.

As the current sheet moves inward, the vertical magnetic field is compressed. Eventually, this causes the outward directed force associated with magnetic pressure to exceed the inward directed force associated with plasma pressure. This leads to a reversal of the motion of the current sheet around $t = 9 \mu\text{s}$, as seen in Fig. 3. As the current sheet moves outward, the force associated with magnetic pressure decreases until around $t = 13 \mu\text{s}$ when the current sheet motion reverses once more. The characteristic time scale for this process is comparable to the period of a standing Alfvén wave with nodes at the flux cores. While inward motion of the current sheet is observed during pull reconnection in experiment (e.g. Ref. 17), multiple reversals of the current sheet motion are atypical.

Rather than the asymmetric inflow that is present in simulations of pull reconnection, it is the outflow that is asymmetric during push reconnection. A pressure buildup on the inboard side of the current sheet develops due to the same volume effects leading to the pressure cavity in pull reconnection. As a result of this pressure buildup, the X-point is located near the outboard side of

the current sheet [as seen in Fig. 4(a)]. Normally, such a pressure buildup would be expected to suppress inward directed outflow. Because the X-point is located near the outboard side of the current sheet, the magnetic tension on the inboard side of the X-point is strong enough to counter the pressure gradient. The magnetic tension on the outboard side of the current sheet is correspondingly weaker, but the pressure force is directed radially outward throughout the current sheet and hence facilitates faster radially outward directed outflow. The net result is that the peak inward and outward directed outflow velocities are similar ($\sim 20 \text{ km s}^{-1}$), although the outward directed outflow is slightly faster. We note also that the flux of material from both sides of the current sheet is approximately the same.

2. Pressure effects, flux availability, and reconnection rate

Experimental results from MRX show that the Sweet-Parker model must be modified to take into account the effects of downstream pressure [45]. We find in this work that outflow confinement affects how quickly the reconnection process can occur. In pull reconnection, plasma is confined between the separatrices and the flux cores. The low available volume results in the high downstream pressure buildup seen in Fig. 2(b), which in turn reduces the reconnection rate. The large downstream pressure of 400 Pa is comparable to the upstream magnetic pressure of 360 Pa and much larger than the initial pressure of 240 Pa or the inflow pressures of 150 Pa (inboard) and 230 Pa (outboard). In push reconnection, downstream plasma is able to expand along the field lines outside the separatrices that surround the flux cores. While a large pressure maximum of 420 Pa is present on the inboard side of the current sheet [see Fig. 4(b)], pressure facilitates outflow on the outboard side rather than impeding it. Hence, pressure effects have less of an impact on the push reconnection rate than the pull reconnection rate.

The time evolution of the reconnection process is also affected by the availability of poloidal flux. In pull reconnection, the amount of flux able to be reconnected is limited by the amount of flux initially available. In push reconnection, this limit does not exist because flux is continually injected into the system via the flux core boundary conditions. This consideration and the confinement properties of the two modes of operation both help explain why push reconnection is quicker than pull reconnection.

3. Toroidal diamagnetic current

In Figs. 2(a) and 4(a), four arms of toroidal current density that extend from the current sheet are apparent. These arms exist along the separatrices and are co-incident with the strong pressure gradients between the upstream and downstream regions. The poloidal mag-

netic field is mostly parallel to the closely packed pressure contours. These arms are regions of high diamagnetic current density, $\mathbf{J}_* = -(\nabla p \times \mathbf{B})/B^2$, which develops through the evolving force balance and facilitates confinement of downstream plasma. The toroidal current along these arms is in the same direction as the current in the reconnection layer.

4. Scalings with driving voltage and resistivity

Global effects (such as driving voltage) and local effects (such as resistivity) both play a role in determining the rate of reconnection and the characteristics of the reconnection layer. In Figs. 5 and 6 we show the results of scaling studies for resistivity η and driving voltage strength V_{loop} measured at $t = 11.2 \mu\text{s}$ when the current sheet is well developed (see Sec. VC1 for a discussion of the reconnection rate as a function of time). The simulations use linear geometry to preserve symmetries and simplify the analysis, but still include the flux cores.

The value for δ is found by fitting the resulting axial magnetic field at $Z = 0$ to the function $B_Z(R) = -B_0 \tanh[(R - R_0)/\delta] + b_1 R$ for pull reconnection and $B_R(Z) = -B_0 \tanh[Z/\delta] + b_1 Z$ for push reconnection (e.g. Ref. 44). As mentioned previously, $L_{0.5}$ is the distance in the outflow direction between the location of peak out-of-plane current density and where the out-of-plane current density reaches half of its strongest value.

In Fig. 5(a), the relation $\delta \propto \eta^{1/2}$ is seen to be valid for both push and pull reconnection. The length $L_{0.5}$ is seen to be nearly constant over an order of magnitude in η in Fig. 5(b), indicating that the length is set by global parameters rather than local parameters in resistive MHD with uniform diffusivity. This is in contrast to experimental results in which the quantity ηL is found to be approximately constant and anomalous resistivity effects cannot be ignored [23]. The aspect ratio of the current sheet is similar for both push and pull reconnection, but the physical dimensions are larger for pull reconnection. The reconnecting electric field is shown in Fig. 5(c) and is compared to the electric field E_{xvac} that would exist at the X-point in the absence of plasma. For both linear and toroidal geometry, E_{xvac} is found through very low Lundquist number simulations ($S \ll 1$) with equivalent drive. The push reconnection rate is higher than the pull reconnection rate due to the effects of geometry and downstream pressure. The difference between the actual reconnection rate and E_{xvac} is due to the finite impedance of the plasma. For a steady-state model, the reconnecting electric field strength by definition must be E_{xvac} ; however, we note that a true steady state cannot exist in this configuration due to the inductive drive, ohmic and viscous heating, and outer boundary conditions.

Fig. 6 shows δ , $L_{0.5}$, and E_{recon} as functions of driving voltage. It is apparent that driving voltage has a strong effect on each of these parameters. The width in Fig. 6(a) decreases with stronger driving voltage, but for

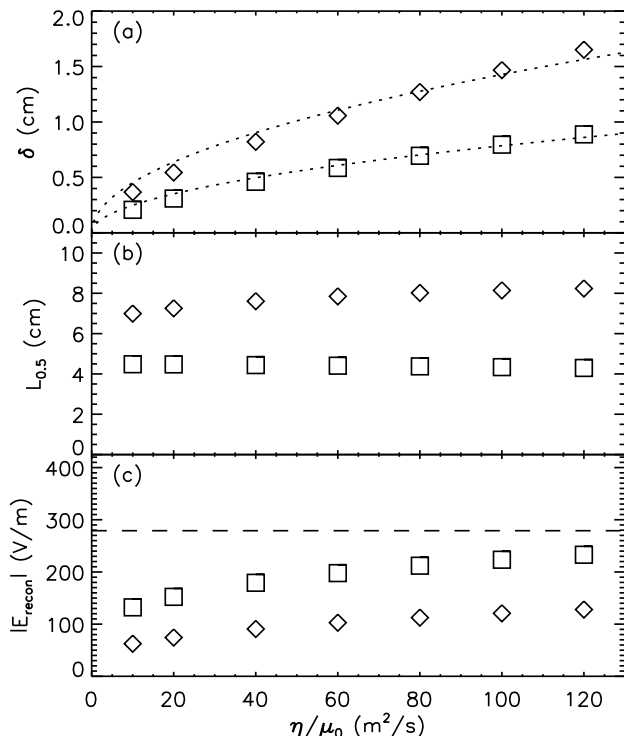


FIG. 5: Comparisons of the (a) thickness δ , (b) length $L_{0.5}$, and (c) reconnecting electric field strength E_{recon} at $t = 11.2 \mu\text{s}$ for linear geometry simulations of push (squares) and pull (diamonds) reconnection using different values of resistivity. For this figure, $V_{\text{loop}} = 1000 \text{ V}$. The dotted lines represent the Sweet-Parker scaling $\delta \propto \eta^{1/2}$ for constant L , V_{in} , and B_{in} , and the dashed line represents the electric field E_{xvac} that would exist at the X-point in the absence of plasma.

strongly driven reconnection, δ becomes less dependent on V_{loop} . In contrast to Fig. 5(b), Fig. 6(b) shows a strong dependence of the length of the current sheet on the driving voltage. This highlights the importance of global effects rather than local effects in determining the length of the current sheet in a resistive MHD model. The reconnecting electric field is found to be roughly proportional to V_{loop} in Fig. 6(c), although still below E_{xvac} . During pull reconnection with $V_{\text{loop}} \gtrsim 1200 \text{ V}$, the length of the current sheet becomes large enough that downstream pressure near the flux core surfaces is able to overcome tension and produce flows that feed back on the current sheet, resulting in reconnection being suppressed.

V. TWO-FLUID NULL-HELICITY SIMULATIONS

In this section, we discuss two-fluid simulations where our Ohm's law is $\mathbf{E} + \mathbf{V} \times \mathbf{B} = \eta \mathbf{J} + (\mathbf{J} \times \mathbf{B} - \nabla p_e) / ne$. The inclusion of the Hall term in the generalized Ohm's law breaks MHD symmetries, and it is now possible to

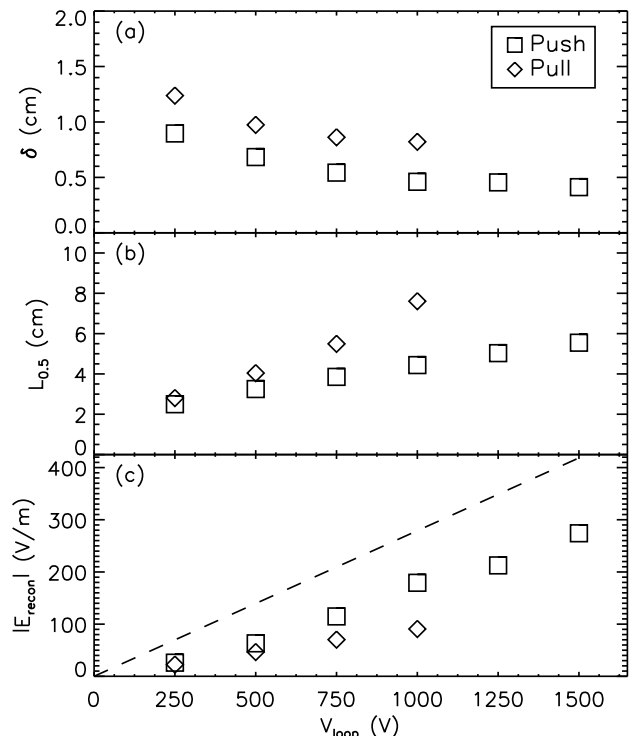


FIG. 6: Comparisons of the (a) thickness δ , (b) length $L_{0.5}$, and (c) reconnecting electric field strength E_{recon} at $t = 11.2 \mu\text{s}$ for linear geometry simulations of push (squares) and pull (diamonds) reconnection using different driving voltage strengths. The current sheet width decreases while the current sheet length and reconnecting electric field both increase. For this figure, $\eta/\mu_0 = 40 \text{ m}^2 \text{ s}^{-1}$. The dashed line represents E_{xvac} as a function of driving voltage.

generate out-of-plane magnetic field during null-helicity reconnection. In particular, all null-helicity cases show the quadrupole magnetic field signature of two-fluid reconnection. In this section we provide an overview of simulations of two-fluid pull and push reconnection, compare the characteristics of two-fluid reconnection to resistive MHD reconnection, and discuss the quadrupole shape and the nature of the electron outflow.

A. Two-fluid pull reconnection

Two-fluid pull reconnection has been studied extensively in the MRX device, resulting in the clearest detections to date of the quadrupole field signature of two-fluid reconnection in a laboratory device [20, 21, 24]. An example quadrupole for a deuterium discharge is seen in Fig. 7(a). Typical measured values from experiment are a maximum quadrupole field strength of $\sim 50 - 100 \text{ G}$ and a reconnecting electric field of $\sim 100 \text{ V/m}$ [21]. There is a tendency for the outboard half of the quadrupole to peak closer to the X-point than the inboard half.

Figures 7(b) and 8 show simulation results from two-

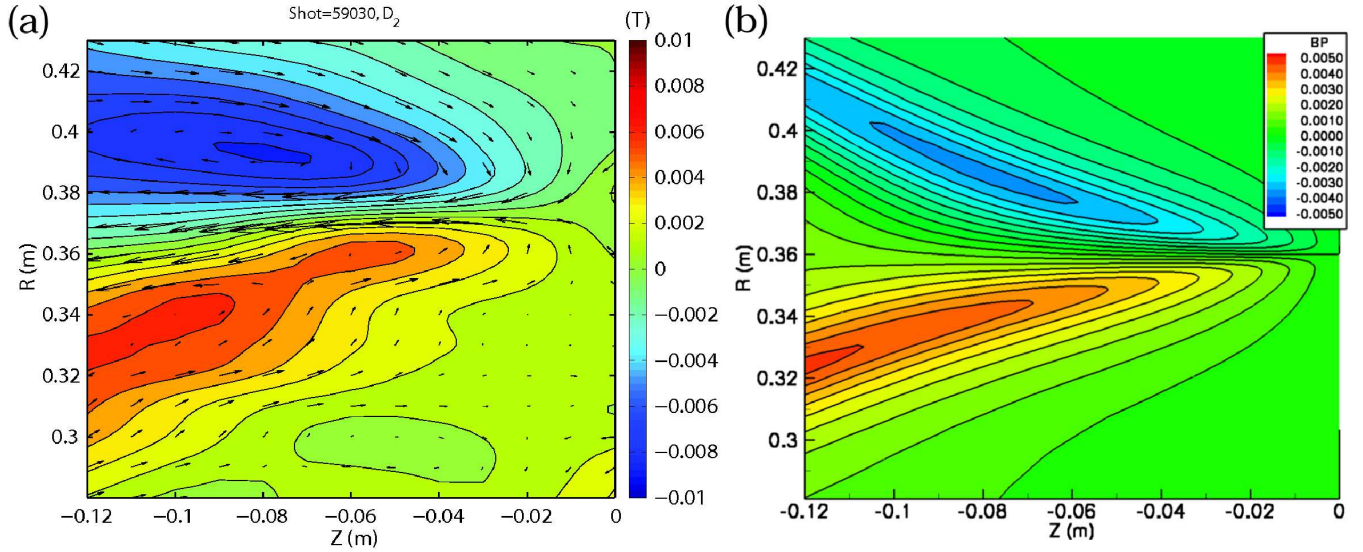


FIG. 7: (a) Experimental results showing toroidal magnetic field contours along with electron velocity vectors during pull reconnection in a typical deuterium discharge in MRX, courtesy of Y. Ren [24]. (b) A closeup of toroidal magnetic field contours during a simulation of two-fluid pull reconnection. Note the difference in the orientation of this figure with respect to Fig. 8.

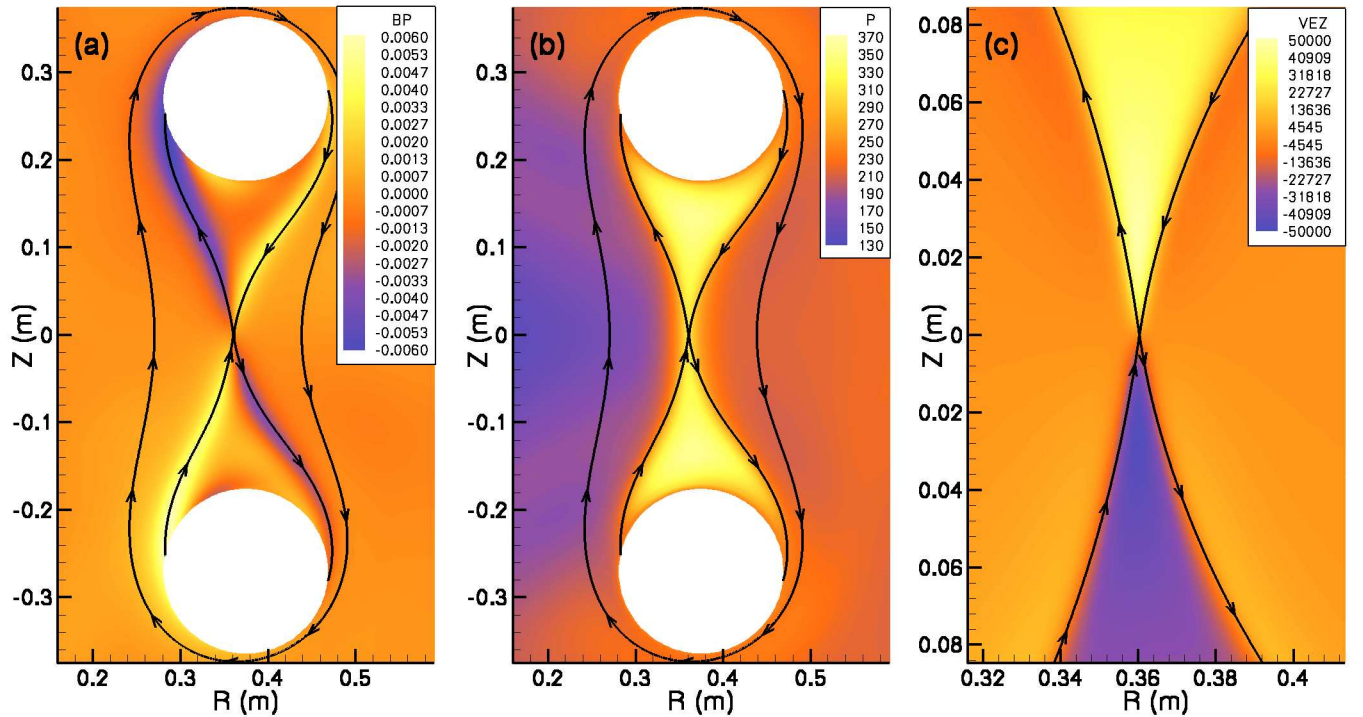


FIG. 8: Simulation results for two-fluid null-helicity pull reconnection with the geometry of MRX, showing (a) the toroidal magnetic field, (b) pressure contours, and (c) the outflow component of the electron velocity, V_{eZ} . The three images also include streamtraces of the poloidal magnetic field. The separatrix is collocated with the quadrupole field and the boundary between the low-pressure inflow and high-pressure outflow regions.

fluid pull reconnection $11.2 \mu\text{s}$ after the start of the simulation. At this time the maximum toroidal field strength is 60 G and the reconnecting electric field is 138 V/m. Due to the effects of toroidicity, the quadrupole is not symmetric to a 180° rotation about the X-point. Similar to experiment, the inboard lobes peak near the flux core surfaces, whereas the outboard lobes peak near the X-point. As in the resistive MHD case, there is a region of low plasma pressure on the inboard side of the current sheet. The buildup of pressure in the outflow region between the separatrices and the flux cores is similar to the MHD result. The separatrices are coincident with the quadrupole field, the region of strongest pressure gradients, and the border between the electron inflow and the electron outflow.

To gauge the impact of parallel heat conduction, simulations using realistic collisional thermal diffusivities of $\chi_{\parallel} = 3 \times 10^5 \text{ m}^2 \text{ s}^{-1}$ and $\chi_{\perp} = 3 \times 10^2 \text{ m}^2 \text{ s}^{-1}$ are compared to simulations using isotropic heat conduction with the thermal diffusivity of $\chi = 400 \text{ m}^2 \text{ s}^{-1}$ listed in Table I. Comparisons are made at $t = 11.2 \mu\text{s}$, after the current sheet is well developed. The range in temperatures in the isotropic simulation is roughly 12 to 19 eV, but is reduced to 14 to 16 eV when strongly anisotropic heat conduction is used. However, pressure and density fields differ by $\lesssim 12\%$ between the two simulations. The reconnection rate is 8% stronger in the anisotropic case. Because pressure gradients in these simulations are driven primarily by variations in density, changing the model of thermal conduction induces only modest changes in the simulation results.

B. Two-fluid push reconnection

Although the quadrupole field has not been observed during the push mode of operation in experiment, comparing simulations of push and pull reconnection helps gauge the importance of global effects on the reconnection process. The out-of-plane quadrupole field that develops is seen in Fig. 9. As in the case for two-fluid pull reconnection, the quadrupole exists along the separatrices, which also form the boundary between the high pressure downstream region and the low pressure upstream region. The width of the quadrupole arms are noticeably smaller than in pull reconnection, and the separatrices surround the flux cores. Throughout the reconnection region there are bulk plasma flows in the toroidal direction. The peak flow strength is typically $6 - 8 \text{ km s}^{-1}$ and is directed in the same direction as the reconnecting current.

As in the resistive MHD case, the outflow is asymmetric. Pressure buildup on the inboard side due to the lesser volume pushes the X-point radially outward, leading to strong tension forces on the inboard side that overcome the stronger pressure gradient. The outward directed outflow is slightly faster than the inward directed outflow. Late in the simulation and despite the asymmetric

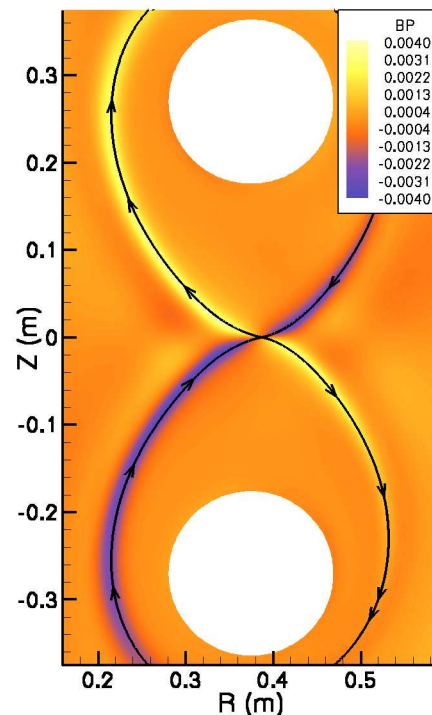


FIG. 9: Toroidal magnetic field contours with a poloidal magnetic field streamtrace during a simulation of two-fluid push reconnection.

outflow, reconnection occurs as quickly as it is driven.

C. Discussion of two-fluid results

1. Comparison with resistive MHD reconnection

Many of the same effects that were discussed in Sec. IV are also present in two-fluid simulations. The position of the current sheet shows a time dependence which is similar to that in the resistive MHD case. This is not unexpected since the pressure asymmetries depend on volume effects which are present regardless of physical model. The diamagnetic arms of toroidal current density are also present in Hall MHD simulations, coincident with the separatrices and the out-of-plane quadrupole field.

The most basic comparison between two-fluid and resistive MHD reconnection is the reconnection rate. In Fig. 10 we show the reconnection rate as a function of time for the simulations discussed in Sections IV and V. We note first that for a given mode of operation, the two-fluid simulation always has a stronger reconnecting electric field than the corresponding resistive MHD simulation. Additionally, for a given physical model, push reconnection is always quicker than pull reconnection. Immediately after reconnection commences, the two-fluid pull reconnection rate follows the two-fluid push reconnection rate closely. However, once effects associated with downstream pressure and flux availability limita-

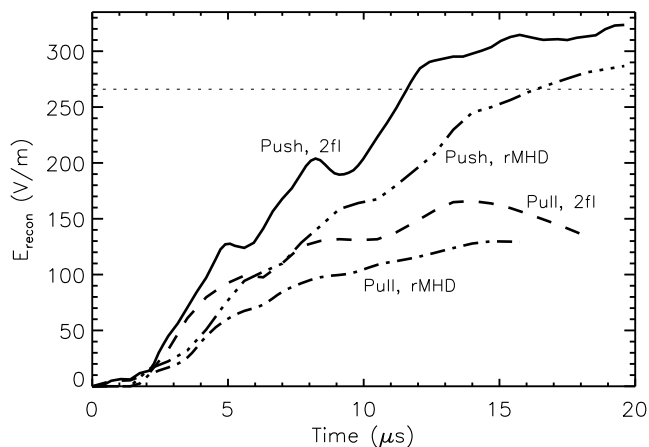


FIG. 10: The reconnecting electric field strength E_{recon} as a function of time for resistive MHD and two-fluid push and pull reconnection. The dotted line shows the electric field strength E_{xvac} that would exist at the initial X-point in the absence of plasma.

tions become important, the two-fluid pull reconnection rate levels off. We note that after early times in these simulations, the mode of operation is more important in determining the reconnection rate than the inclusion of two-fluid effects in the generalized Ohm's law.

Also plotted in Fig. 10 is the electric field strength E_{xvac} that would exist at the X-point were the plasma not present. At $12 \mu\text{s}$, we see that the reconnecting electric field for two-fluid push reconnection exceeds E_{xvac} , but immediately begins to level off. Because of the pileup of flux at previous times, the reconnection rate can exceed E_{xvac} for some time. After an initial transient, reconnection is essentially occurring as quickly as it is driven. Effects associated with downstream pressure and flux availability prevent the reconnecting electric field strength from approaching E_{xvac} during simulations of pull reconnection.

2. Toroidal flows

Toroidal flows are present in simulations of both two-fluid push and pull reconnection with peak magnitudes of up to $V_i \sim 20 \text{ km s}^{-1}$. The flow is in the same direction as the reconnecting current and is almost the magnitude of the diamagnetic drift velocity. Experimental results during pull reconnection with Helium have shown a peak toroidal velocity of several kilometers per second with the rotation predominantly on the outboard side of the current sheet [10], whereas results with Hydrogen show the toroidal flow peaking near the current sheet center with flows up to 12 km s^{-1} .

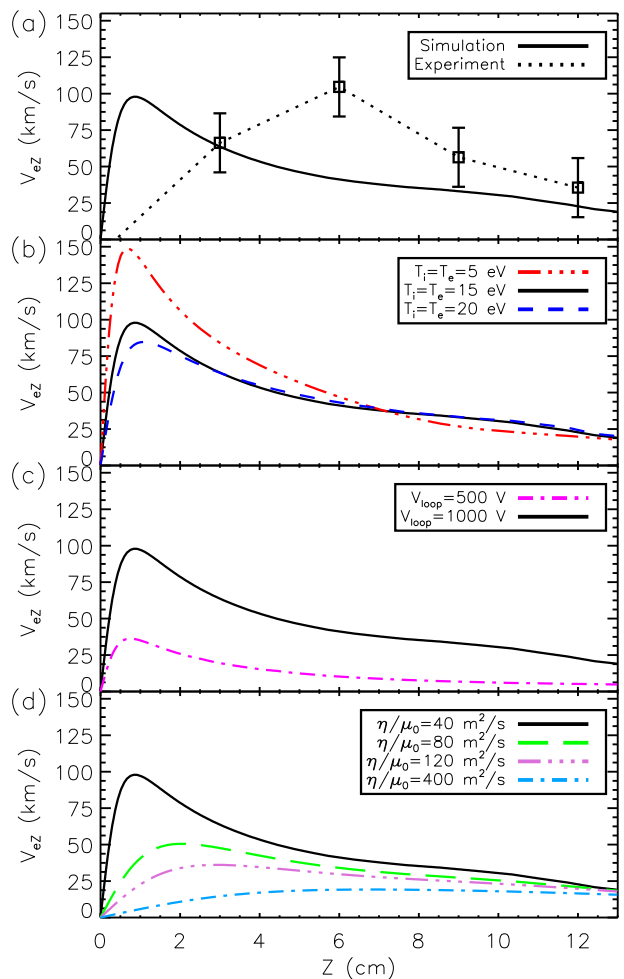


FIG. 11: The outflow component of electron velocity during a linear geometry simulation of two-fluid pull reconnection. In (a), a comparison is made to an equivalent experimental result (data courtesy of Y. Ren [24]). In (b), (c), and (d), comparisons of electron outflow profiles are made for different initial temperatures, driving voltage strengths, and resistivities. Unless noted, $\eta/\mu_0 = 40 \text{ m}^2 \text{ s}^{-1}$.

3. Electron velocity profile

The separation of electron and ion flows plays an important role in two-fluid reconnection, so we now compare V_e profiles with experiment. Fig. 8(c) shows contours of the outflow component of electron velocity during two-fluid pull reconnection, V_{eZ} . The peak electron speed occurs at very short distances from the X-point along each of the outflow paths. This is expected for two-fluid null-helicity reconnection. The net flux of electrons at each value of Z in this region is approximately constant, which can be interpreted as a direct result of whistler physics controlling the shape of the reconnection outflow. As the length scale perpendicular to the outflow decreases closer to the X-point, the outflow velocity increases proportionately.

Experimental results have found that the electron outflow is superAlfvénic and peaks at a distance of $1 - 1.5 c/\omega_{pi}$ away from the X-point [24]. Figure 11(a) shows a comparison of the electron outflow profiles between a linear geometry simulation of two-fluid pull reconnection and experimental data. In contrast to experiment, the peak outflow in simulation is located very close to the X-point.

This discrepancy in the electron outflow profile may be due to physics not contained within our two-fluid model. However, some insight into what sets the electron outflow profile can be gleaned from scaling studies of initial temperature, driving voltage strength, and resistivity. Figure 11(b) shows that while the position of the peak electron outflow is not greatly affected by initial temperature, higher initial temperatures correspond to weaker peak outflows. This highlights the role downstream pressure plays in determining the nature of the electron outflow. Figure 11(c) shows that stronger driving voltages lead to much stronger electron outflows with peaks slightly further from $Z = 0$. Figure 11(d) shows that significantly larger global resistivity leads to slower outflows with peaks located significantly further from the X-point. Short of invoking anomalous resistivity or hyperresistivity models to mimic non-fluid physics, we surmise that the two-fluid model plus uniform resistivity does not reproduce the broad electron outflow acceleration produced in MRX.

4. Electron outflow opening angle

Also of interest is the opening angle of the electron outflow. In Fig. 8(c), the electron outflow opening half-angle is measured to be $\sim 10^\circ$ for two-fluid pull reconnection. A decrease in the initial density by a factor of two results in a much wider cone, typically with a half-angle of $\sim 20^\circ$. Lowering the driving voltage also has the effect of increasing the half-angle to $\sim 20^\circ$. Resistivity has the effect of blurring the boundary between the electron inflow and the electron outflow. A change in the ion species in simulation does not result in a significant change in outflow angle. A recent work by Singh [46] argues that in the whistler regime, the electron outflow opening half-angle matches the linear group velocity cone angle of 19.5° . We note that close to the reconnection region, we have observed no electron outflow opening angles $\gtrsim 20^\circ$. However, experimental results in Fig. 4.19 of Ref. 24 show that the half-angle between the separatrices ranges from 15° to 30° , depending on the ion species. For deuterium, the range is from 15° to 20° .

5. Quadrupole shape

The quadrupole shapes are directly compared between experiment and simulation in Fig. 7. Neither of these results are symmetric to a 180° rotation about the cen-

ter of reconnection [see also Fig. 8(a)]. Because linear geometry simulations show a symmetric quadrupole field with the X-point at the midpoint between the two flux cores, we conclude the asymmetry in simulation is due to toroidicity. While the quadrupole lobes appear thinner and more clearly separated in simulation than in experiment, the peak magnitude of the outboard quadrupole is located near $Z = 8$ cm in both the simulation and experimental results. In contrast, a clear local maximum for the inboard quadrupole lobes is not within the region plotted in both Fig. 7(a) and Fig. 7(b). In simulation, the inboard quadrupole lobes are strongest near the flux core surfaces. We note, however, that toroidal fields induced during the plasma formation process may also influence the experimental results.

During pull reconnection, the quadrupole field is strongly affected by the flux cores. While in push reconnection the quadrupole is everywhere concave towards the flux cores, it turns concave away from the flux cores near the X-point in pull reconnection [see Figs. 8(a) & 9]. This indicates that, especially for pull reconnection, the flux core positions noticeably affect the spatial distribution of the quadrupole field. We also note that (1) the pull quadrupole lobes have greater breadth than the push quadrupole lobes, (2) the quadrupole is located along the separatrix for both push and pull reconnection, and (3) the quadrupole peak strength is greater during pull reconnection than push reconnection despite that the push reconnection rate is greater than the pull reconnection rate.

VI. CO- AND COUNTER-HELICITY TWO-FLUID RESULTS

In the simulations reported in Sections IV and V, the electric field applied on the flux core surfaces is purely toroidal, and hence the flux cores do not directly induce toroidal field. The out-of-plane magnetic fields that are present in two-fluid simulations are generated through in-plane electric fields in the plasma. It is important to note again that for null-helicity resistive MHD reconnection, there is no in-plane electric field and hence no out-of-plane magnetic field is able to develop. In this section we consider the effects of inducing a toroidal field directly from the flux cores. In co-helicity merging, the induced toroidal field is in the same direction from both flux cores. In counter-helicity reconnection, the induced toroidal field is in opposite directions. We will show that asymmetry due to the Hall effect leads to asymmetric outflow that then feeds back on the reconnection layer through pressure gradients.

A. Two-Fluid Co-Helicity Push Reconnection

Figure 12 shows the results of two-fluid co-helicity (guide field) push reconnection in a linear geometry sim-

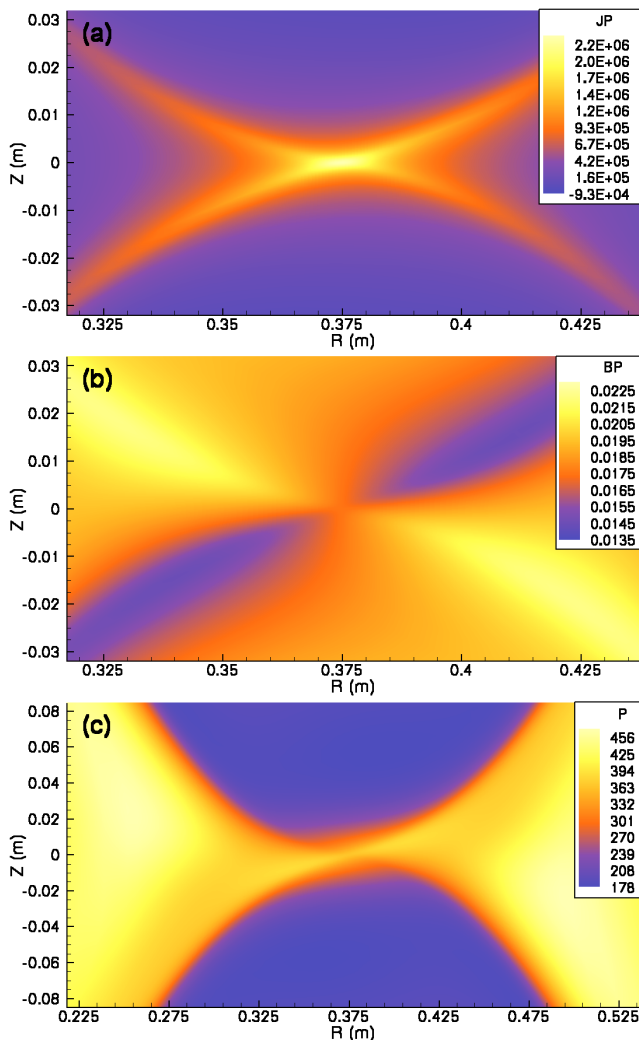


FIG. 12: Out-of-plane current density (a), out-of-plane magnetic field (b), and plasma pressure (c) during a linear geometry simulation of two-fluid co-helicity (guide field) push reconnection.

ulation. From Fig. 12(a), we see that the current sheet is tilted with respect to $Z = 0$. From Figs. 12(b) and 12(c), we see that the out-of-plane magnetic field pattern and plasma pressure distributions are also tilted. These features are not present during resistive MHD simulations. This tilting of the current sheet structure has not been unambiguously identified in MRX, but has been observed in experiments at the CS-3D device during guide field experiments with heavy ions [47], as well as in previous simulations (e.g. Refs. 48, 49).

To gain insight into the origin of this tilting effect, consider that during two-fluid antiparallel reconnection, there are strong in-plane currents associated with the electron outflow. Artificially imposing a guide field leads to a vertical (Z) component of the Hall electric field in the outflow region, seen for our simulation in Figure 13(a). This vertical Hall electric field represents a Lorentz force that acts in opposite directions on the ions and the elec-

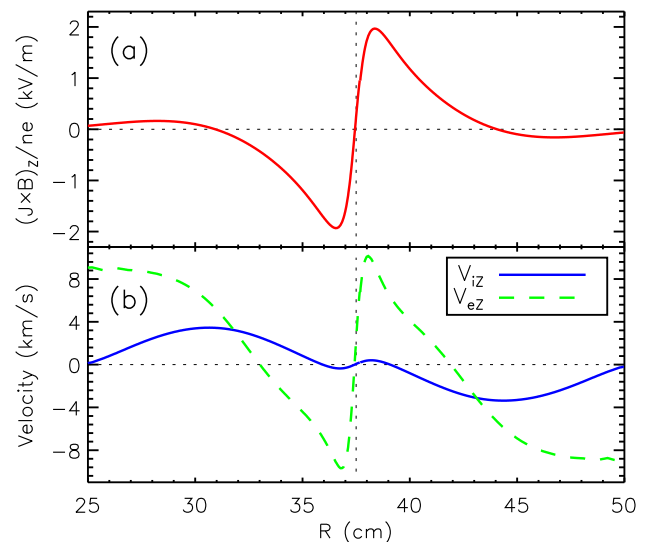


FIG. 13: The vertical component of the Hall electric field (a), and the vertical components of the ion and electron velocities V_{iz} and V_{ez} (b) along $Z = 0$ during a linear geometry simulation of two-fluid co-helicity push reconnection.

trons on each side of the current sheet, resulting in different signs of the Z component of velocity for each species along $Z = 0$ as seen in Fig. 13(b). The magnetic field is carried in the direction of electron motion on scales $\lesssim c/\omega_{pi}$, resulting in a tilted current sheet.

Associated with the tilting of the current sheet is tilting of the pressure contours, as shown in Fig. 12(c). This can be understood in terms of the vertical component of the ion and electron velocity along $Z = 0$, shown in Fig. 13(b). To the immediate left (right) of the X-point, the ions exhibit a small downward (upward) component of velocity that is directly due to the tilted nature of the current sheet. At distances further out, ions show a positive Z component of velocity for $R < 37.5$ cm and a negative Z component of velocity for $R > 37.5$ cm. This velocity profile is a direct result of the mechanism discussed above, and leads to the distorted pressure contours.

B. Two-fluid Counter-Helicity Push Reconnection

Recent experimental results in MRX show that the X-point exhibits a radial shift in position associated with the Hall effect during counter-helicity push reconnection [25]. Differences in the reconnection rate and the downstream pressure are also observed for reversed toroidal field directions. In these results, the surface containing reconnecting field lines is rotated, and the electron velocity associated with the reconnecting current has a radial component. The magnetic field configuration is carried by the electrons in the radial direction, resulting in a shift in position of the X-point. As pointed out in Ref. 25, this effect is related to the formation of the quadrupole field during null-helicity merging. However,

a strict comparison with a tilted quadrupole does not take into account the axisymmetric nature of the configuration. For example, in the extreme case of the opposing toroidal fields being much stronger than the opposing poloidal fields, quadrupole formation is disallowed because it would require a poloidal field that changes direction in the toroidal angle.

The shift in position of the X-point does not require the effects of toroidicity, and so to simplify the analysis of this symmetry breaking mechanism we first discuss linear geometry simulations of counter-helicity push reconnection. Resistive MHD simulations of counter-helicity push reconnection do not show the development of this asymmetry. When two-fluid physics is added to the time advance during the middle of a simulation, the asymmetry develops quickly as the magnetic field becomes tied to the electron fluid. As the radial shift develops, the asymmetric outflow also becomes noticeable. This ties the asymmetry to the Hall effect.

Fig. 14 shows current density contours (a) and pressure contours (b) for a simulation with two-fluid physics included from the beginning. The flux cores are positioned at $R = 0.375$ m, indicating that the current sheet is shifted to the left (with respect to Fig. 14). There is a corresponding buildup of pressure on the side from which the current sheet was shifted. A quadrupole field is still present when viewed in a rotated reference frame (not shown). The electron outflow is predominantly towards the left and the ion outflow is predominantly towards the right. The pressure buildup on the right corresponds to the ion (bulk plasma) outflow, and the shift of the current sheet to the left corresponds to the electron outflow.

Several effects exist that facilitate the asymmetric flow pattern and pressure distribution. (1) High B_Z magnetic pressure closer to the X-point on the left slows outflow aimed in that direction [25]. (2) Higher magnetic tension on the right increases outflow directed to the right. (3) As the plasma attempts to settle into equilibrium, the result is a diamagnetic ion flow to the right above and below the current sheet. All of these effects are present in this simulation and enhance asymmetric outflow in the same direction.

The asymmetric outflow is best understood by comparing the plasma pressure, magnetic tension, and magnetic pressure terms in the momentum equation along $Z = 0$, as shown in Fig. 15. On the far left, magnetic pressure dominates and limits the ability of plasma to escape the reconnection region. This facilitates the development of a small region of enhanced plasma pressure that acts on the outflow to the left to cancel forces resulting from magnetic tension close to the X-point. On the right hand side, magnetic tension is stronger because the current sheet is pulled to the left. Magnetic and plasma pressure are largely flat for approximately 5 cm, and magnetic tension overwhelms all other forces in the region to the right of the current sheet.

The above analysis investigates the flow along $Z = 0$. However, diamagnetic effects are apparent in the flow

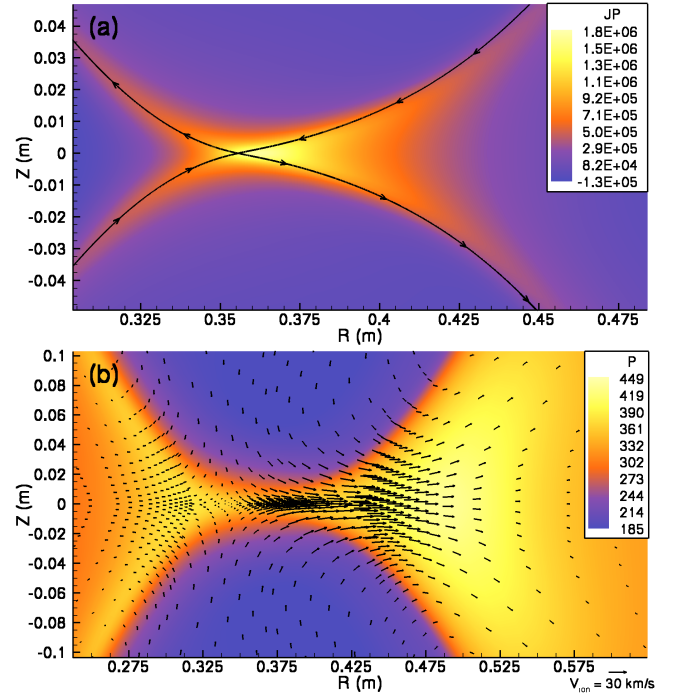


FIG. 14: Out-of-plane current density along with a magnetic field streamtrace of the separatrix (a), and plasma pressure with ion velocity vectors (b) during a simulation of two-fluid counter-helicity push reconnection performed in linear geometry to remove the effects of toroidicity. The out-of-plane magnetic field induced by the flux cores is out of the page for $Z > 0$ and into the page for $Z < 0$. Note that in (a) the X-point is shifted to the left of $R = 0.375$ (the position of the flux core centers) and that in (b) there is strong ion outflow towards the right that leads to the asymmetric pressure buildup.

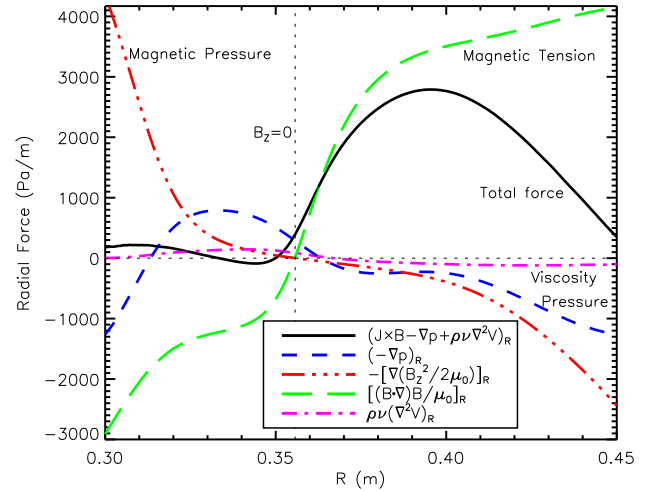


FIG. 15: Terms in the R -component of the momentum equation along $Z = 0$ m are compared for a simulation of two-fluid counter-helicity push reconnection using linear geometry. The X-point position is shifted to the left of $R = 0.375$ m due to the Hall effect.

patterns above and below the current sheet. In its general form, the diamagnetic drift is given by

$$\mathbf{V}_{*j} = -\frac{\nabla p_j \times \mathbf{B}}{q_j n B^2}. \quad (10)$$

The diamagnetic drift has been studied previously in the context of reconnection as a suppression mechanism when there is a density gradient in the inflow direction [35]. Immediately above and below the current sheet, radial derivatives are small, so

$$\mathbf{V}_* \approx -\frac{1}{2qnB^2} \left(\hat{R} B_\phi \frac{\partial p_{tot}}{\partial Z} - \hat{\phi} B_R \frac{\partial p_{tot}}{\partial Z} \right), \quad (11)$$

where for our single-temperature model, the subscript j indicating species has been dropped. The pressure in the current sheet is a factor of 1.5-2 higher than the pressure a few centimeters above and below. This jump in pressure occurs within a length scale of 1-2 cm, corresponding to an extremely large localized pressure gradient. In this region, a typical value of the vertical pressure gradient is $\partial p / \partial Z \approx 7 - 10 \times 10^3$ Pa/m, significantly larger than most other pressure gradients found in the system. For the values found at $(R, Z) = (0.36, -0.01)$, we find that the ions have a rightward magnetic drift of order 30 km/s, and the electrons have a leftward magnetic drift with the same magnitude. The drift for each species is in the same direction both above and below the current sheet. When the reconnection plane is no longer in the poloidal plane, pressure gradients are no longer in the same plane as the reconnecting magnetic fields and these additional diamagnetic drift effects must be considered.

Along $Z = 0$, the diamagnetic drift in the radial direction is small. The pressure gradient opposes the ion outflow but is shallow compared to $(\mathbf{J} \times \mathbf{B})_R$. This latter term plays the dominant role in accelerating the bulk plasma outflow in this region where the vertical pressure gradient goes to zero. It should be noted that in simulations with $\beta = 0$, the X-point is still shifted and there is asymmetric outflow even without the diamagnetic drift. However, above and below the current sheet the diamagnetic drift significantly alters the flow pattern.

This discussion of asymmetry due to the Hall effect has not invoked toroidicity. In the discussion of push reconnection in Sec. IV, we noted that the lesser volume available on the inboard side of the current sheet leads to a fast buildup of pressure that pushes the X-point radially outward. Hence, during two-fluid counter-helicity push reconnection in toroidal geometry, symmetry is broken due to both toroidicity and the Hall effect. Depending on the orientation of the toroidal field, these symmetry breaking mechanisms can either work together or oppositely.

Fig. 16 shows the effects of the combination of these two symmetry breaking mechanisms on the toroidal current density, the plasma pressure, and the radial velocity along $Z = 0$. Using the nomenclature from Ref. 25 for two-fluid simulations, case O shows a radially outward

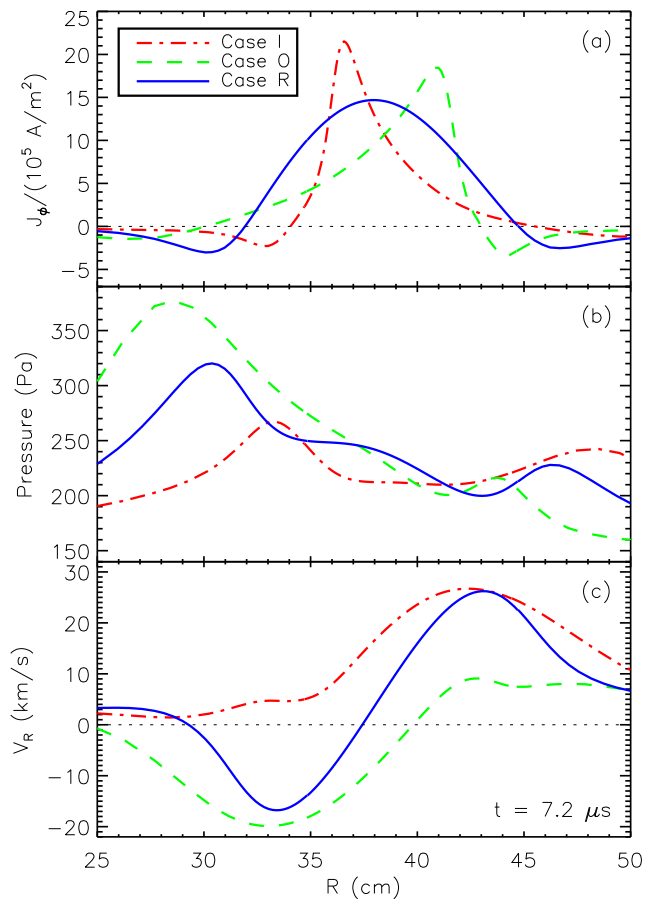


FIG. 16: Toroidal current density (a), plasma pressure (b), and radial velocity (c) as functions of radius during counter-helicity push reconnection using toroidal geometry. Symmetry breaking is due to both toroidicity and the Hall effect. Cases I and O refer to two-fluid simulations of counter-helicity push reconnection showing an inward and outward radial shift, respectively. Case R refers to the resistive MHD equivalent of case I.

shift of the X-point, while case I shows an inward shift of the X-point. In the poloidal slice shown in Fig. 1, case O (case I) has toroidal field in the out-of-page (in-page) direction for $Z > 0$ and in the in-page (out-of-page) direction for $Z < 0$. Case R is a resistive MHD simulation where the sign of B_ϕ does not affect the result. The initial conditions, plasma parameters, and driving voltage strengths are identical for all three cases.

The Hall symmetry breaking is most apparent in Fig. 16(a). Cases I and O display the expected behavior for out-of-plane current density, clearly showing an inward shift of the X-point for case I and an outward shift of the X-point for case O, both relative to case R. Figs. 16(b) and 16(c) show that the pressure distribution and the radial velocity profile are strongly affected by both toroidicity and Hall symmetry breaking. In case O, both the Hall effect and toroidicity are acting to increase the outflow in the inboard direction. As a result, the pressure

profile across the reconnection region decreases almost monotonically and the radially inward outflow is much stronger than the radially outward outflow. In case I, the Hall effect is trying to push the outflow in the outboard direction while toroidicity is trying to push the outflow in the inboard direction. The pressure profile is much flatter than case O, but the outflow is predominantly in the radially outward direction.

VII. SUMMARY AND CONCLUSIONS

In this paper we report on simulations of two-fluid reconnection that fully incorporate the Hall term in the generalized Ohm's law while using the geometry of an actual reconnection experiment. Both the push and pull modes of the Magnetic Reconnection Experiment (MRX) are simulated with and without two-fluid effects to investigate the impact of global effects on the reconnection process. The two-fluid model used in NIMROD includes resistivity, the Hall term, and the electron pressure gradient in the generalized Ohm's law, but not electron inertia. A uniform resistivity is used in the reconnection region, thus ignoring effects associated with anomalous resistivity.

Throughout this paper, pressure effects are found to be an important intermediary between small and large scales. Asymmetries in the inflow and outflow directions feed back on the reconnection process through large scale pressure gradients. During pull reconnection, the inboard side of the current sheet is depleted of density more quickly than the outboard side due to the small volume available on the inboard side. Consequently, the current sheet displays a radially inward motion after reconnection commences which stops when magnetic pressure becomes large enough to counterbalance the plasma pressure gradient. A similar effect occurs during push reconnection. Whereas pull reconnection has asymmetric upstream boundary conditions, push reconnection has asymmetric downstream boundary conditions. A significant pressure buildup occurs on the inboard side of the current sheet. While such a pressure buildup would normally be expected to strongly suppress radially inward directed outflow, the X-point position is shifted to the outboard side of the current sheet. This strengthens the magnetic tension on the inboard side of the current sheet, thus allowing strong inward directed outflow to be maintained.

A comparison of the reconnection rates for resistive MHD and two-fluid push and pull reconnection shows that in these simulations, geometry plays a more substantial role in determining the reconnection rate than the inclusion of the Hall term. For a given mode of operation, the inclusion of the Hall term increases the reconnection rate by $\sim 25\%$, but for a given physical model, push reconnection is $\sim 50\%$ quicker than pull reconnection. The difference is attributed to the importance of downstream pressure and the limited flux available to re-

connect during the pull mode of operation. During push reconnection, the reconnection rate plateaus at a value slightly over the electric field strength that would exist in the absence of plasma, indicating that for this case reconnection is occurring as quickly as it is driven. Pull reconnection, however, is limited by flux availability and is eventually quenched by downstream pressure.

In addition to the well-known quadrupole field present during null-helicity merging, there are additional two-fluid effects which manifest themselves during co-helicity and counter-helicity push reconnection. When a guide field is present during co-helicity merging, the electrons in the outflow region experience a Lorentz force in the Z direction. The electrons carry the magnetic field, resulting in a tilt of the current sheet. The ion flow is also affected, resulting in an asymmetric pressure distribution due to the Z component of the ion outflow. During simulations with toroidicity, the current sheet position is shifted from $Z = 0$.

Simulations of two-fluid counter-helicity push reconnection using linear geometry are performed to analyze the development of asymmetric outflow that is associated with the radial shift in position of the X-point seen in Ref. 25. On the side to which the X-point is shifted, the dominant force is magnetic pressure, which is important due to both the compression of B_Z and to the simple fact that the radial shift in position of the X-point means that the strong vertical magnetic field is closer. On the side from which the X-point is shifted, forces associated with magnetic and plasma pressure are small, while the force due to magnetic tension is large. The consequences are that outflow on the side to which the X-point is shifted is suppressed, while outflow on the side from which the X-point is shifted is enhanced. Additionally, diamagnetic drifts of ions and electrons above and below the current sheet help facilitate this asymmetric flow pattern. When a toroidal geometry is used, symmetry breaking due to volume effects acts to push the X-point outward and increase pressure on the inboard side of the current sheet, as in null-helicity cases. Hence, depending on the orientation of B_ϕ above and below the current sheet, the Hall symmetry breaking can work with symmetry breaking due to toroidicity, or against it.

Acknowledgments

The authors are grateful for discussions with researchers associated with MRX, especially M. Yamada, H. Ji, Y. Ren, S. Gerhardt, M. Inomoto, E. Belova, A. Kuritsyn, and S. Dorfman. We acknowledge helpful comments from M. Brown, P. Cassak, V. Lukin, V. Mirnov, S. Prager, M. Swisdak, and E. Zweibel. Finally, we thank the other members of the NIMROD Team for code development contributions that helped make this work possible. This research is supported by the National Science Foundation, Grant No. PHY-0215581 (PFC: Center for Magnetic Self-Organization in Laboratory and Astro-

physical Plasmas).

-
- [1] J. Birn, J. F. Drake, M. A. Shay, B. N. Rogers, R. E. Denton, M. Hesse, M. Kuznetsova, Z. W. Ma, A. Bhattacharjee, A. Otto, et al., *J. Geophys. Res. [Space Phys.]* **106**, 3715 (2001).
- [2] B. N. Rogers, R. E. Denton, J. F. Drake, and M. A. Shay, *Phys. Rev. Lett.* **87**, 195004 (2001).
- [3] M. E. Mandt, R. E. Denton, and J. F. Drake, *Geophys. Res. Lett.* **21**, 73 (1994).
- [4] U. O. Sonnerup, in *Solar system plasma physics. Volume 3. (A79-53667 24-46) Amsterdam, North-Holland Publishing Co., 1979, p. 45-108.* (1979), vol. 3, pp. 45–108.
- [5] H. Karimabadi, J. D. Huba, D. Krauss-Varban, and N. Omidi, *Geophys. Res. Lett.* **31**, 7806 (2004).
- [6] M. Yamada, H. Ji, S. Hsu, T. Carter, R. Kulsrud, N. Bretz, F. Jobes, Y. Ono, and F. Perkins, *Phys. Plasmas* **4**, 1936 (1997).
- [7] M. Yamada, H. Ji, S. Hsu, T. Carter, R. Kulsrud, Y. Ono, and F. Perkins, *Phys. Rev. Lett.* **78**, 3117 (1997).
- [8] H. Ji, M. Yamada, S. Hsu, and R. Kulsrud, *Phys. Rev. Lett.* **80**, 3256 (1998).
- [9] S. C. Hsu, G. Fiksel, T. A. Carter, H. Ji, R. M. Kulsrud, and M. Yamada, *Phys. Rev. Lett.* **84**, 3859 (2000).
- [10] S. C. Hsu, T. A. Carter, G. Fiksel, H. Ji, R. M. Kulsrud, and M. Yamada, *Phys. Plasmas* **8**, 1916 (2001).
- [11] T. Carter, H. Ji, F. Trintchouk, M. Yamada, and R. Kulsrud, *Phys. Rev. Lett.* **88** (2002).
- [12] T. A. Carter, M. Yamada, H. Ji, R. M. Kulsrud, and F. Trintchouk, *Phys. Plasmas* **9**, 3272 (2002).
- [13] F. Trintchouk, M. Yamada, H. Ji, R. M. Kulsrud, and T. A. Carter, *Phys. Plasmas* **10**, 319 (2003).
- [14] A. Kuritsyn, M. Yamada, S. Gerhardt, H. Ji, R. Kulsrud, and Y. Ren, *Phys. Plasmas* **13**, 5703 (2006).
- [15] H. Ji, S. Terry, M. Yamada, R. Kulsrud, A. Kuritsyn, and Y. Ren, *Phys. Rev. Lett.* **92**, 115001 (2004).
- [16] H. Ji, M. Yamada, S. Terry, R. Kulsrud, Y. Ren, and A. Kuritsyn, in *Plasmas in the Laboratory and in the Universe: New Insights and New Challenges*, edited by G. Bertin, D. Farina, and R. Pozzoli (2004), vol. 703 of *American Institute of Physics Conference Series*, pp. 437–442.
- [17] S. Dorfman, H. Ji, M. Yamada, Y. Ren, S. Gerhardt, R. Kulsrud, B. McGeehan, and Y. Wang, in *Theory of Fusion Plasmas*, edited by O. Sauter (2006), vol. 871 of *American Institute of Physics Conference Series*, pp. 306–311.
- [18] S. P. Gerhardt, E. Belova, M. Inomoto, M. Yamada, H. Ji, Y. Ren, and A. Kuritsyn, *Phys. Plasmas* **13**, 2508 (2006).
- [19] S. P. Gerhardt, E. V. Belova, M. Yamada, H. Ji, M. Inomoto, Y. Ren, and B. McGeehan, *Phys. Rev. Lett.* **99**, 245003 (2007).
- [20] Y. Ren, M. Yamada, S. Gerhardt, H. Ji, R. Kulsrud, and A. Kuritsyn, *Phys. Rev. Lett.* **95**, 055003 (2005).
- [21] M. Yamada, Y. Ren, H. Ji, J. Breslau, S. Gerhardt, R. Kulsrud, and A. Kuritsyn, *Phys. Plasmas* **13**, 2119 (2006).
- [22] A. Kuritsyn, Ph.D. thesis, Princeton University (2005).
- [23] A. Kuritsyn, H. Ji, S. Gerhardt, H. Ren, and M. Yamada, *Geophys. Res. Lett.* **34**, L16106 (2007).
- [24] Y. Ren, Ph.D. thesis, Princeton University (2007).
- [25] M. Inomoto, S. P. Gerhardt, M. Yamada, H. Ji, E. Belova, A. Kuritsyn, and Y. Ren, *Phys. Rev. Lett.* **97**, 135002 (2006).
- [26] W. H. Matthaeus, C. D. Cothran, M. Landreman, and M. R. Brown, *Geophys. Res. Lett.* **32**, 23104 (2005).
- [27] F. S. Mozer, S. D. Bale, and T. D. Phan, *Phys. Rev. Lett.* **89**, 015002 (2002).
- [28] T.-H. Watanabe, T. Hayashi, T. Sato, M. Yamada, and H. Ji, *Phys. Plasmas* **6**, 1253 (1999).
- [29] V. S. Lukin, G. Qin, W. H. Matthaeus, and M. R. Brown, *Phys. Plasmas* **8**, 1600 (2001).
- [30] V. S. Lukin and S. C. Jardin, *Phys. Plasmas* **10**, 3131 (2003).
- [31] D. Schnack, I. Lottati, Z. Mikić, and P. Satyanarayana, *J. Comput. Phys.* **140**, 71 (1998).
- [32] R. L. Stenzel and W. Gekelman, *J. Geophys. Res. [Space Phys.]* **86**, 649 (1981).
- [33] M. Ugai, *Phys. Plasmas* **7**, 867 (2000).
- [34] K. Kondoh, M. Ugai, and T. Shimizu, *Advances in Space Research* **33**, 794 (2004).
- [35] M. Swisdak, B. N. Rogers, J. F. Drake, and M. A. Shay, *J. Geophys. Res. [Space Phys.]* **108**, 23 (2003).
- [36] M. G. Linton, *J. Geophys. Res. [Space Phys.]* **111**, 12 (2006).
- [37] P. A. Cassak and M. A. Shay, *Phys. Plasmas* **14**, 102114 (2007).
- [38] J. E. Borovsky and M. Hesse, *Phys. Plasmas* **14**, 102309 (2007).
- [39] C. R. Sovinec, A. H. Glasser, T. A. Gianakon, D. C. Barnes, R. A. Nebel, S. E. Kruger, D. D. Schnack, S. J. Plimpton, A. Tarditi, and M. S. Chu, *J. Comput. Phys.* **195**, 355 (2004).
- [40] C. R. Sovinec, D. D. Schnack, A. Y. Pankin, D. P. Brennan, H. Tian, D. C. Barnes, S. E. Kruger, E. D. Held, C. C. Kim, X. S. Li, et al., *Journal of Physics Conference Series* **16**, 25 (2005).
- [41] D. D. Schnack, D. C. Barnes, D. P. Brennan, C. C. Hegna, E. Held, C. C. Kim, S. E. Kruger, A. Y. Pankin, and C. R. Sovinec, *Phys. Plasmas* **13**, 058103 (2006).
- [42] C. D. Cothran, M. Landreman, M. R. Brown, and W. H. Matthaeus, *Geophys. Res. Lett.* **32**, 3105 (2005).
- [43] C. R. Sovinec, D. D. Schnack, D. C. Barnes, and D. P. Brennan, *Bull. Am. Phys. Soc.* **51**, 166 (2006).
- [44] M. Yamada, H. Ji, S. Hsu, T. Carter, R. Kulsrud, and F. Trintchouk, *Phys. Plasmas* **7**, 1781 (2000).
- [45] H. Ji, M. Yamada, S. Hsu, R. Kulsrud, T. Carter, and S. Zaharia, *Phys. Plasmas* **6**, 1743 (1999).
- [46] N. Singh, *J. Geophys. Res. [Space Phys.]* **112**, 7209 (2007).
- [47] A. G. Frank, S. Y. Bogdanov, G. V. Dreiden, V. S. Markov, and G. V. Ostrovskaya, *Phys. Lett. A* **348**, 318 (2006).
- [48] M. Hesse, K. Schindler, J. Birn, and M. Kuznetsova, *Phys. Plasmas* **6**, 1781 (1999).
- [49] P. L. Pritchett and F. V. Coroniti, *J. Geophys. Res. [Space Phys.]* **109**, 1220 (2004).